Ocean Engineering 357 (2026) 125586

Contents lists available at ScienceDirect

Ocean Engineering

journal homepage: www.elsevier.com/locate/oceaneng

Research paper

Research on active vibration and noise control of piezoelectric propeller blades based on the FNNPID-FxLMS algorithm

Xudong Zhang [a], Pengxiang Zhao [a], Xin Lan [b], Weikai Shi [a], Liwu Liu [a,*], Yanju Liu [a,**], Jinsong Leng [b]

[a] Department of Astronautical Science and Mechanics, Harbin Institute of Technology, Harbin, 150001, People's Republic of China
[b] Centre for Composite Materials and Structures, Harbin Institute of Technology, Harbin, 150080, People's Republic of China

ARTICLE INFO

Keywords:
Piezoelectric propeller blades
Vibration control
Noise control
FNNPID-FxLMS algorithm

ABSTRACT

This study proposed an active control method, namely FNNPID-FxLMS, which combined a fuzzy neural network PID controller with the FxLMS algorithm to address the problem of low-frequency vibration and radiated noise of piezoelectric propeller blades. First, the dynamic characteristics of the blade system were accurately obtained through an offline identification method. A closed-loop hardware-in-the-loop control platform was established to simulate the vibration response of the blades under practical operating conditions. The experimental results showed that, under constant-speed propulsion conditions, the RMS values of vibration were significantly reduced at advance speeds of 6, 12, and 18 knots, while noise reduction at 18 knots was limited. In addition, under multi-line disturbance conditions, the FNNPID-FxLMS algorithm also effectively suppressed vibration and noise, with the maximum reduction in noise RMS reaching 80.3% and the maximum reduction in vibration RMS reaching 52.7%. These results indicated that the FNNPID-FxLMS algorithm exhibited significant advantages in vibration and noise control, including faster convergence speed, lower steady-state error, and stronger robustness. This study provided an effective solution for the active control of propeller vibration and noise in ships and offered support for the application of control technologies in related fields.

Nomenclature

FNNPID-FxLMS	Fuzzy neural network PID filtered-x least mean square	$W(k)$	Control filter
$[M]$	Mass matrix	$y(k)$	Secondary path output signal
$[C]$	Damping matrix	$C(k)$	Secondary path transfer function
$[K]$	Stiffness matrix	$C'(k)$	Secondary path estimation
$\{x''(t)\}$	Acceleration response	c	Filter weight vector
$\{x'(t)\}$	Velocity response matrix	$s(k)$	Combined sensor signal
$\{x(t)\}$	Displacement response matrix	$e(k)$	Error signal
$\{F(t)\}$	External excitation force matrix	$d(k)$	Desired signal
$\{\varphi_r\}$	The r-th mode shape	μ	Step size
x_s	Excitation-point response	$X_f(k)$	Reference signal autocorrelation matrix
x_e	Observation-point response	e	Bias
H_{es}	FRF between excitation-point and observation-point	e_c	Bias rate
$[H]$	Transfer function matrix	I	Input of the network layer
		O	Output of the network layer
		k_0	Acoustic wave number
		r	Propeller radius
		d	Receiver–source distance
		F_i	Unsteady blade force
		$x(k)$	Reference signal
		x_i	Input of the first layer
		c_{ij}	Center of the membership function
		b_{ij}	Width of the membership function
		λ_l	Firing strength of the fuzzy rule
		η_{kl}	Connection weight

(*continued on next column*)

(*continued*)

1. Introduction

During the propulsion process, a ship propeller not only overcomes fluid resistance to generate thrust but is also subjected to the combined action of complex unsteady hydrodynamic forces and excitations transmitted through the shafting–hull system. These excitations induce periodic or multi-mode vibrations of the blades, which subsequently radiate noise into the surrounding water and become critical factors

* Corresponding author.
** Corresponding author.
E-mail addresses: liulw@hit.edu.cn (L. Liu), yj_liu@hit.edu.cn (Y. Liu).

https://doi.org/10.1016/j.oceaneng.2026.125586
Received 3 February 2026; Received in revised form 2 April 2026; Accepted 11 April 2026
Available online 18 April 2026

influencing both crew health and overall ship comfort. Traditional passive vibration reduction and noise isolation methods are typically effective only within narrow frequency ranges and are insufficient to meet the requirements of multi-condition and broadband noise suppression. Active vibration and noise control (AVC/ANC) technologies, owing to their real-time adaptability, gradually become key approaches to addressing such challenges. In particular, with the advancement of piezoelectric materials and embedded hardware, coupling active control with piezoelectric propeller blades in practical propulsion systems has become a research frontier in ship noise control. Although existing studies have made some progress in propeller fluid–structure interaction modeling, system identification, and control strategies, achieving simultaneous suppression of vibration and noise under full-scale blade operating conditions still remains a challenge. Channel delay, system nonlinearity, and the strong coupling between vibration and noise cause traditional control algorithms to suffer from slow convergence, large steady-state errors, and unstable control outputs. Therefore, the core problem of this study is how to establish a high-precision system model under typical operating conditions and to achieve vibration and noise control of the blades through improved control strategies.

The study of propeller vibration and noise had long received extensive attention. In the field of fluid–structure interaction and acoustic modeling, scholars gradually revealed the dynamic characteristics of blades under unsteady hydrodynamic forces and the mechanisms of radiated noise by employing analytical methods, finite element/boundary element methods, and hybrid numerical approaches (Sujbert; Aboutiman et al.; Watanabe and Prasad; Zhang et al.a; Chen et al.). Some works verified the accuracy of simulations based on experiments or scaled models (Gao et al.; Lu et al.), while other studies established near- and far-field acoustic radiation models for practical propulsion systems and conducted further investigations. In the field of system identification, sweep-frequency tests combined with modal analysis were widely employed to extract transfer functions and system models (Li et al.a; Lopes and Gerald; Ouyang et al.; Xu et al.a). Further improvements included the introduction of ARX/NARX and Volterra models to enhance identification accuracy under conditions of time delay and weak nonlinearity (Wu et al.a; Duan et al.; Yang et al.a). At the same time, studies also emphasized the influence of sensor placement and regularization methods on model observability and robustness (Zhang et al.b). Such work provided applicable models for the controller design of complex coupled systems. In the development of active control algorithms, FxLMS and its improved versions consistently served as the research core. Early studies compared the convergence and steady-state performance of single-channel and multi-channel FxLMS, as well as their normalized and variable step-size variants (Yang et al.b). For scenarios involving time delays and non-minimum phase channels, researchers introduced Kalman filtering and predictive control to improve broadband suppression performance (Kamaldar et al.; Song et al.). Under multi-harmonic excitation conditions, multi-reference decoupling and subband parallel updating strategies demonstrated outstanding effectiveness (Sharma et al.a; Jamshidi and Jafari; Park et al.). In addition, some studies also addressed practical issues such as sensor saturation, channel mismatch, and online compensation (Xu et al.b; Zhang et al.c; Tian et al.). Intelligent and robust control methods gradually emerged in recent years. Fuzzy logic, neural networks, and ANFIS were employed for gain scheduling and nonlinear compensation to enhance stability and adaptability under operating condition switching and time-varying environments (Chai et al.a; Wan et al.; Xu et al.c; Singh et al.a; Cheng et al.). Integrated approaches, such as fuzzy–sliding mode or optimal control, also achieved significant effectiveness in disturbance rejection and constraint handling (Zhang et al.d; Li et al.b). At the same time, by combining passive or semi-active measures (e.g., piezoelectric shunting, damping layers, and periodic struts), hybrid control realized superior vibration and noise reduction performance over broadband ranges (Al-Souqi et al.; Huang et al.; Muthalif et al.; Callipari et al.; Zhang et al.e; Zhang et al.f). Research progress was also made on the nonlinear characteristics of piezoelectric materials (Wu et al.b; Lin et al.), which were widely applied in the driving field. These achievements indicated that coupling intelligent methods with the traditional FxLMS framework provided distinct advantages. In addition, ARX/NARX, RLS, and Bayesian/Kalman approaches were applied to path identification and steady-state analysis under channel uncertainty and background noise (Yang et al.c; Wang et al.; Sharma et al.b; Zhang and Zhu, 2023; Singh et al.b; Pulthasthan and Pota; Zhang et al.g). These methods ensured the stability of closed-loop systems in low signal-to-noise ratio and time-varying environments. In terms of engineering applications and system verification, research already covered subsystems such as propulsion shafting, propeller blades, cabin sections, and pipelines. Experimental and prototype tests demonstrated that multi-channel sensing and actuation layouts effectively suppressed transverse or axial vibrations (Yue et al.; Aktas and Esen). Variable stiffness and magnetic suspension support technologies significantly reduced displacement and resonance responses (Xiong et al.). Hybrid control methods achieved engineering validation in suppressing aft system far-field noise and pipeline structural noise (Luo et al.; Geng et al.; Chai et al.b). Some studies also explored fault-tolerant control and the optimization of sensor–actuator layouts (Przybylski and Kulinski; Jiang et al.; Jalalnezhad).

In summary, existing studies had established a complete chain in mechanism modeling, system identification, and control strategies; however, research on the simultaneous active control of vibration and noise of propeller blades under typical operating conditions remained limited. This gap provided the innovation space for the FNNPID-FxLMS algorithm and its experimental validation proposed in this paper. Section 2 introduced the blade dynamics, acoustic radiation modeling, and the derivation of the control algorithm. Section 3 described the construction of the experimental platform and the testing scheme. Section 4 presented and analyzed the experimental results under typical operating conditions. Section 5 summarized the main findings of this study and outlined future prospects for its extension to multi-channel coupling and more complex nonlinear environments.

2. Piezoelectric propeller blade theory

2.1. Constitutive equations

The equations of motion for an N-degree-of-freedom system in the physical coordinate system are expressed as:

$$[M]\{x''(t)\}+[C]\{x'(t)\}+[K]\{x(t)\}=\{F(t)\} \tag{1}$$

In the equation, $[M]$ denotes the mass matrix of the system, $[C]$ denotes the damping matrix, $[K]$ denotes the stiffness matrix, $\{x''(t)\}$ denotes the acceleration response vector, $\{x'(t)\}$ denotes the velocity response vector, $\{x(t)\}$ denotes the displacement response vector, and $\{F(t)\}$ denotes the external excitation force vector of the system.

By applying the Fourier transform, the coordinate transformation leads to the equations of motion in the modal coordinate system:

$$\left(-\omega^2[M]+j\omega[C]+[K]\right)\{X(j\omega)\}=\{F(j\omega)\} \tag{2}$$

The r-th order modal differential equation is expressed as:

$$\left(-\omega^2[M]_r+j\omega[C]_r+[K]_r\right)q_r=\{\varphi_r\}^T\{F(j\omega)\} \tag{3}$$

Where $\{\varphi_r\}$ denotes the r-th mode shape. Let $[\varphi]=[\{\varphi_1\}\{\varphi_2\}\cdots\{\varphi_n\}]$, When the system is subjected to an excitation $\{F(j\omega)\}=[0\cdots0\cdots f(j\omega)\cdots 0\cdots0]$ at point s, it follows that:

$$q_r=\frac{\varphi_{sr}f_s(j\omega)}{([K]_r-\omega^2[M]_r+j\omega[C]_r)} \tag{4}$$

The response of the system at any point e is expressed as:

$$x_e(j\omega)=\sum_{r=1}^{n}\varphi_{er}q_r=\frac{\varphi_{er}\varphi_{sr}f_s(j\omega)}{([K]_r-\omega^2[M]_r+j\omega[C]_r)} \tag{5}$$

The frequency response function between point s and point e is expressed as:

$$H_{es}(j\omega)=\sum_{r=1}^{n}\frac{\varphi_{er}\varphi_{sr}}{([K]_r-\omega^2[M]_r+j\omega[C]_r)} \tag{6}$$

The transfer function matrix of the system is expressed as:

$$[H(j\omega)]=\sum_{r=1}^{n}\frac{1}{([K]_r-\omega^2[M]_r+j\omega[C]_r)}\begin{bmatrix}\varphi_{1r}\varphi_{1r} & \varphi_{1r}\varphi_{2r} & \cdots & \varphi_{1r}\varphi_{nr}\\ \varphi_{2r}\varphi_{1r} & \varphi_{2r}\varphi_{2r} & \cdots & \varphi_{2r}\varphi_{nr}\\ \vdots & \vdots & \vdots & \vdots\\ \varphi_{nr}\varphi_{1r} & \varphi_{nr}\varphi_{2r} & \cdots & \varphi_{nr}\varphi_{nr}\end{bmatrix} \tag{7}$$

Each row or column of the above transfer function matrix corresponds to the relevant parameters of the modal matrix of the propeller blades.

For the low-frequency noise generated by vibration during propeller propulsion, the unsteady force acts as a compact acoustic source, and the noise is considered to be directly radiated from the unsteady force. Therefore, given the unsteady force of propeller propulsion, the radiated noise can be calculated as follows:

$$p_a=-jk_0F_i\frac{d}{r}\frac{e^{-j\omega(t-r/c_0)}}{4\pi r} \tag{8}$$

In the equation, k_0 is the acoustic wave number. For a given operating condition, it is determined by the acoustic frequency and sound speed, and is not treated in this study as an independent flow-field variable. $\frac{\omega}{c_0}$ denotes the ratio of frequency to sound velocity, r denotes the propeller radius, and d denotes the distance from the acoustic source to the receiving point with the source taken as the origin. F_i denotes the unsteady force acting on the blade, which can be taken as the maximum axial unsteady force, as shown in Fig. 1. In the three-dimensional multi-degree-of-freedom propeller system, the external excitation force vector of the system is denoted as $\{F(t)\}=[0,F_i,0]^T$.

2.2. Governing equations

The active control algorithm is the core of an active control system, and the quality of the algorithm determines the performance of the entire system. The earliest active control algorithm is the least mean-square (LMS) algorithm based on the stochastic gradient method, which is characterized by finding the optimal weight vector through simple and efficient recursive computation. However, because the physical channel between the secondary path and the error sensor is neglected, a time delay problem arises. To overcome the adverse effects of the secondary path, accelerate convergence, and reduce adaptive steady-state error, the filtered-x least mean-square (FxLMS) algorithm becomes one of the most commonly used control strategies, as shown in Fig. 2.

If a control system has I reference sensors, J secondary sources, and K error sensors, then the numbers of primary and secondary channels are $I\times J$ and $J\times K$. $x(n)$ denotes the acquired reference signal, and the reference signal vector received by the I-th reference sensor is assumed to be:

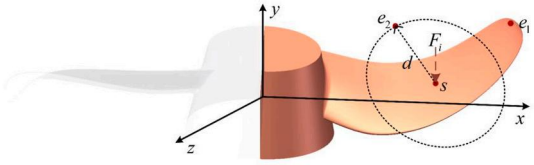

Fig. 1. Schematic diagram of the propeller blade.

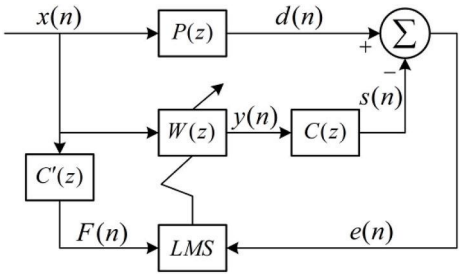

Fig. 2. Block diagram of the FxLMS algorithm.

$$X(n)=[x_1(n),x_2(n),\cdots,x_I(n)] \tag{9}$$

The reference signal vector of the i-th reference sensor is expressed as:

$$x_i(n)=[x_i(n),x_i(n-1),\cdots,x_i(n-L+1)]^T \tag{10}$$

$W(n)$ denotes the control filter with a length of L, where the weight coefficient of the j-th filter is expressed as:

$$W_j(n)=\left[w_{j,1}(n),w_{j,2}(n),\cdots,w_{j,L}(n)\right]^T \tag{11}$$

The output signal of the j-th secondary path at time n is $y_j(n)$, which is obtained as:

$$y_j(n)=\sum_{l=1}^{L}w_{j,l}(n)^*x(n-l+1)=w_j^T{}^*x(n) \tag{12}$$

Let $C(n)$ denote the transfer function of the secondary path, and let $C'(n)$ denote the estimated value of $C(n)$ obtained through secondary path identification. The transfer function of the secondary path is expressed as:

$$C(n)=\begin{pmatrix}c_{11}(n) & c_{12}(n) & \cdots & c_{1K}(n)\\ c_{21}(n) & c_{22}(n) & \cdots & c_{2K}(n)\\ \vdots & \vdots & \vdots & \vdots\\ c_{J1}(n) & c_{J1}(n) & \cdots & c_{JK}(n)\end{pmatrix} \tag{13}$$

Each element $c_{jk}(n)$ represents the weight vector of a filter with length L, which is denoted as:

$$c_{jk}=\left[\omega_{jk1}(n),\omega_{jk2}(n),\cdots,\omega_{jkL}(n)\right]^T \tag{14}$$

$s(n)$ denotes the output secondary signal:

$$s(n)=[s_1(n),s_2(n),\cdots,s_K(n)]^T \tag{15}$$

The signal $s_k(n)$ received by the k-th sensor, which is the superposition of the J-th output after passing through the secondary path, is expressed as:

$$s_k(n)=\sum_{j=1}^{J}c_{jk}(n)^*y_j(n) \tag{16}$$

The multi-channel system achieves the cancellation of the primary signal by minimizing the sum of squares of error signals. After the secondary signal cancels the desired signal, the error signal $e(n)$ is generated. The weight vector composed of the outputs of the error sensors is denoted as:

$$e(n)=d(n)-s(n) \tag{17}$$

Where $d(n)$ denotes the desired signal, and the filter weight vector is expressed as:

$$W(n+1)=W(n)-2\mu X_f(n)e(n) \tag{18}$$

Where μ denotes the step size, and $X_f(n)$ denotes the autocorrelation matrix of the reference signal:

$$X_f(n) = C'(n) * X(n) \tag{19}$$

To better compensate for the coupled components in the control system and to make it more suitable for time-varying and nonlinear objects, this study proposes the FxLMS algorithm combined with the fuzzy neural network PID (FNNPID-FxLMS) algorithm, as shown in Fig. 3.

As shown in Fig. 4, the first layer is the input layer, and each node is directly connected to the input variables. This layer also serves as the direct data transmission layer, which does not require data processing and directly assigns values to the inputs. The layer contains two nodes, namely the error e and the rate of change of error e_c.

$$\begin{cases} I_i^{(1)} = x_i \\ O_i^{(1)} = I_i^{(1)} \end{cases} \tag{20}$$

In the equation, I and O denote the input and output of the network layer, respectively, and the superscript denotes the number of the network layer; $i = 1, 2$.

The second layer is the fuzzification layer, which performs fuzzification processing on the input variable x_i from the first layer. Each node in this layer represents a linguistic variable value.

$$\begin{cases} I_i^{(2)} = O_i^{(1)} \\ O_{ij}^{(2)} = \exp\left[-\left(x_i - c_{ij}\right)^2 \Big/ b_{ij}^2 \right] \end{cases} \tag{21}$$

In the equation, c_{ij} denotes the center of the membership function, and b_{ij} denotes the width of the membership function.

The third layer is the fuzzy inference layer, which performs matching of the corresponding fuzzy rules. The combinations among the fuzzy nodes generate the applicability λ_l of the corresponding fuzzy rules, enabling fuzzy operations among the neural nodes. Each node in this layer corresponds to a fuzzy rule.

$$\begin{cases} I_{ij}^{(3)} = O_{ij}^{(2)} \\ O_l^{(3)} = \lambda_l = I_{1j}^{(3)} \times I_{2j}^{(3)} \end{cases} \tag{22}$$

The fourth layer is the output layer, which computes the fuzzy quantities obtained from fuzzy inference and generates the final output of the fuzzy neural network. This layer contains three output nodes, each corresponding to the variation of one parameter in the PID controller.

$$\begin{cases} I_l^{(4)} = O_l^{(3)} \\ O_k^{(4)} = \sum_k \sum_l \eta_{kl} I_l^{(4)} \end{cases} \tag{23}$$

In the equation, η_{kl} denotes the connection weight between the fuzzification layer and the output layer; $k = 1, 2, 3$.

The variations of the three parameters of the PID in the final output are expressed as:

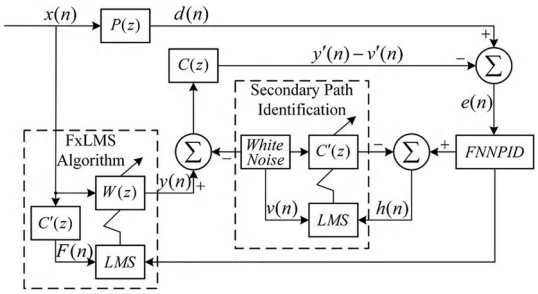

Fig. 3. Block diagram of the FNNPID-FxLMS algorithm.

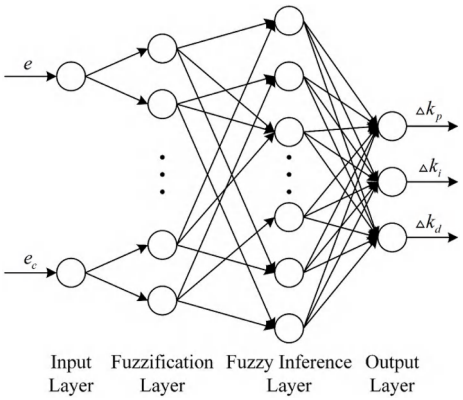

Fig. 4. Structural diagram of the fuzzy PID neural network.

$$\begin{cases} \Delta k_p = O_1^{(4)} \\ \Delta k_i = O_2^{(4)} \\ \Delta k_d = O_3^{(4)} \end{cases} \tag{24}$$

In the FNNPID module, the inputs of the fuzzy neural network are the error e and the rate of change of error e_c, and the outputs are the incremental adjustments Δk_p, Δk_i, and Δk_d of the PID controller. The fuzzy rules are designed based on the tradeoff among response speed, overshoot suppression, and steady-state accuracy. When the error is large, k_p is increased to accelerate the response. When the error changes rapidly, k_d is increased to improve damping and suppress oscillation. When the error becomes small and tends to be stable, k_i is increased appropriately to reduce the steady-state error. Through fuzzy inference and neural-network weight adaptation, the PID parameters are adjusted online to match the time-varying dynamic characteristics of the blade system.

The computation process of the fuzzy PID neural network consists of two steps: forward calculation of the network and backward error propagation with weight adjustment. This process is repeated until the error is eliminated. When the input signal passes through one layer, the weight of the corresponding node is calculated based on the current weight and the activation function. The output result is then transferred to the next layer. When the network output is inconsistent with the desired output, the error signal between the output and the desired output is propagated backward, and the returned error is used as the basis for weight adjustment. This control system adjusts the output signal according to the weights to achieve the minimum mean square error.

PID control eliminates steady-state error and improves response speed; however, to enhance the performance of the PID controller, it is necessary to adjust the relationship among the proportional, integral, and derivative units. The fuzzy neural network is capable of approximating any nonlinear function and can be used to identify the optimal PID parameters through the network. Therefore, the FNNPID-FxLMS algorithm not only provides the advantage of fast parameter convergence but also achieves multi-channel decoupling control based on the principle of optimal control.

3. Preparation

The original-size single E1619 blade was obtained through casting, as shown in Fig. 5. The blade was further processed using a five-axis CNC machine to refine the positions for the driver installation and vibrator connection.

To reduce the influence of fixed boundary conditions on the vibration control experimental results, a single propeller blade was bolted to a rib plate, and the blade structure was rigidly connected to a cast iron platform. Surrounding plates were welded around the blade and

Fig. 5. E1619 blades and casting site.

connected to the cast iron platform, after which water was injected to form a small hydrostatic test tank for the propeller blade, thereby establishing an active control platform for propeller vibration and noise, as shown in Fig. 6. The rotation radius of the blade was 1560 mm, and the blade profile was E1619, cast from H26 brass alloy. An exciter (model JZK-50; rated output force: 500 N, maximum amplitude: ±12.5 mm) was mounted vertically at two-thirds of the blade chord length to induce vibration, with a force sensor (model CL-YD-2311; force measurement range: ±10 kN, sensitivity error: ≤2%) connected in series with the actuator rod. Two-thirds of the blade chord length corresponds to the region of significant bending and torsional strain in the propeller blade. It is also the position where the blade experiences the maximum unsteady fluid pulsating force from the surrounding flow field. A piezoelectric actuator and a preloading device were embedded in series at one-third of the blade chord length. An eddy-current displacement sensor (model ZA-21; measurement range: 1 mm, sensitivity error: ≤2%) was installed at the blade tip to measure vibration displacement at that point. In addition, a noise sensor (model HBK8103; Frequency range: 0.1 Hz to 180 kHz) was placed in the hydrostatic water near the trailing edge of the blade to measure the radiated noise caused by blade vibration.

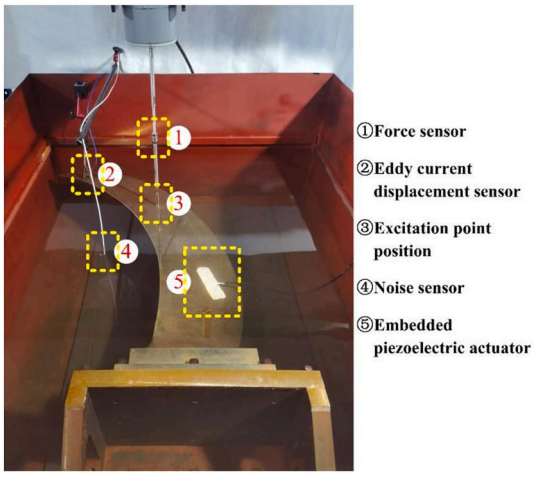

Fig. 6. Experimental platform for active vibration and noise control of piezoelectric propeller blades.

The experiment adopted a closed-loop control method, and its principle was illustrated in Fig. 7. The hardware-in-the-loop control platform was equipped with an 8-core real-time controller (model PXIe-8881; running the Linux RT real-time operating system), a 2-channel 24-bit analog output dynamic signal generator (model PXIe-4463), and a 16-channel 24-bit dynamic signal acquisition card (model PXIe-4497). Real-time data exchange between the control platform and the host computer was achieved. The host computer generated analog signals, which were converted by the dynamic signal generator and amplified by a power amplifier (model YE5874A; rated output power: 810 W) to produce voltage signals that drove the exciter, thereby inducing vibration in the propeller blade. The noise sensor acquired radiated noise, while the eddy-current displacement sensor collected vibration data. The vibration displacement at the end of the blade is used as the input to the FNNPID-FxLMS controller. The noise signal is not directly used as a control input, but serves as a performance evaluation metric for acoustic suppression. The control system generated real-time control signals through the dynamic signal generator, which, after amplification by a piezoelectric ceramic power amplifier (model E00. C3; average power per channel: 7 W to 35 W), drove the piezoelectric actuator to suppress blade vibration. Real-time data exchange was continuously carried out, and the algorithm was executed with a step size of 1 ms.

This study mainly investigated the active control of low-frequency vibration and its radiated noise in piezoelectric propeller blade structures. First, the sweep-frequency method was employed to obtain the dynamic response of the blade structure, and the dynamic characteristics of the FNNPID-FxLMS algorithm were analyzed based on numerical simulations. Subsequently, closed-loop vibration control experiments were conducted on the piezoelectric propeller blade structure using the control algorithm, and vibration and radiated noise data of the structure were collected.

4. Results and discussion

4.1. Active vibration control simulation of piezoelectric propeller blades

Before conducting the simulation of the blade system, a sweep-frequency test was carried out to obtain a more accurate understanding of the blade's dynamic response. The purpose of this test was to observe the dynamic behavior of the blade under excitations at different frequencies and thereby determine its response characteristics at various frequencies. The experimental data analyzed through the offline identification method accurately described the dynamic characteristics of the blade and were further used to derive the transfer function of its

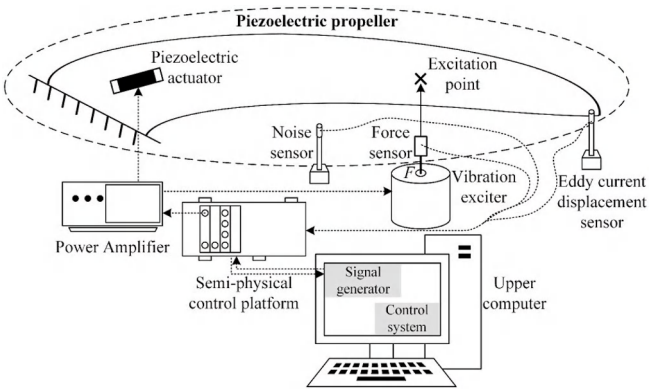

Fig. 7. Schematic diagram of the closed-loop control method.

discrete system.

Fig. 8 shows the offline identification process and the dynamic characteristic analysis results of the blade system. The figure presents the dynamic responses of the blade under excitations at different frequencies, and the transfer function was obtained through data fitting. This analysis not only provided the frequency response characteristics of the blade but also revealed key dynamic parameters of the blade system, such as damping ratio and natural frequency. The discretization of the transfer function made the dynamic model of the blade more suitable for digital simulation.

Fig. 8 shows the identified dynamic characteristics of the propeller blade system. The time-domain results in subfigure (a) indicate that the output generally follows the input excitation. Subfigure (b) presents the error curve of the FIR fitting result, showing that the fitting error is mainly concentrated in the transient stage. The delay estimation in subfigure (c) shows that the correlation peak is located near zero lag, indicating a small system delay. The impulse response in subfigure (d) confirms that the system has finite dynamic memory. The Bode magnitude and phase results in subfigure (e) and subfigure (f) show that the FIR and ARX models capture the main frequency-response characteristics of the system, although deviations remain in some frequency bands. The step responses in subfigure (g) further reflect the dynamic characteristics of the identified models. As shown in subfigure (h), the coherence is high in the low-frequency range and decreases gradually with increasing frequency. The pole-zero distribution in subfigure (i) indicates that the system has clear resonant characteristics and provides the basis for the subsequent simplified modeling and controller design.

The FxLMS algorithm was simple to describe and easy to understand, and it was regarded as one of the most widely used adaptive control algorithms in the field of active vibration control. In particular, the algorithm required only multiplication and addition operations, which matched well with the operating structure of standard PXIe hardware. This compatibility facilitated its adaptation and implementation in practical engineering application systems.

As shown in Fig. 9, the FNNPID-FxLMS algorithm proposed in this study used the FxLMS algorithm as the core and introduced the FNNPID module and the Reset & Uniformization module. The FNNPID part provided nonlinear adaptive gain adjustment, compensating for the problems of slow convergence and large steady-state error encountered by the traditional FxLMS algorithm in time-varying or nonlinear noise environments. The Reset & Uniformization part normalized and limited the output of the FNNPID to prevent excessive control effort from causing filter divergence. The clock mechanism ensured “reset” or “re-uniformization” at fixed intervals, thereby enhancing the robustness of the system.

Building on the advantages of the FxLMS algorithm, the FNNPID-FxLMS algorithm employed a neural network with PID structural constraints to provide adaptive compensation, allowing the system to reach steady state more quickly during startup and operating condition changes. The fuzzy neural network offered nonlinear mapping capability, which compensated for the performance loss of the FxLMS algorithm under the assumption of linearity when the channel exhibited slight nonlinearity. Compared with the FxLMS algorithm, the FNNPID-FxLMS algorithm achieved faster convergence, greater stability, and improved robustness against time-varying and nonlinear conditions.

For the discrete system with time delay, the transfer function was identified offline and denoted as $G(s) = \frac{0.5684s^2 - 1.0623s + 0.5111}{s^2 - 1.9303s + 0.9392}$. The amplitude of the higher-order modes is relatively small and have relatively minor effect on the vibration control performance within the targeted frequency band. The second-order model captures the domi-

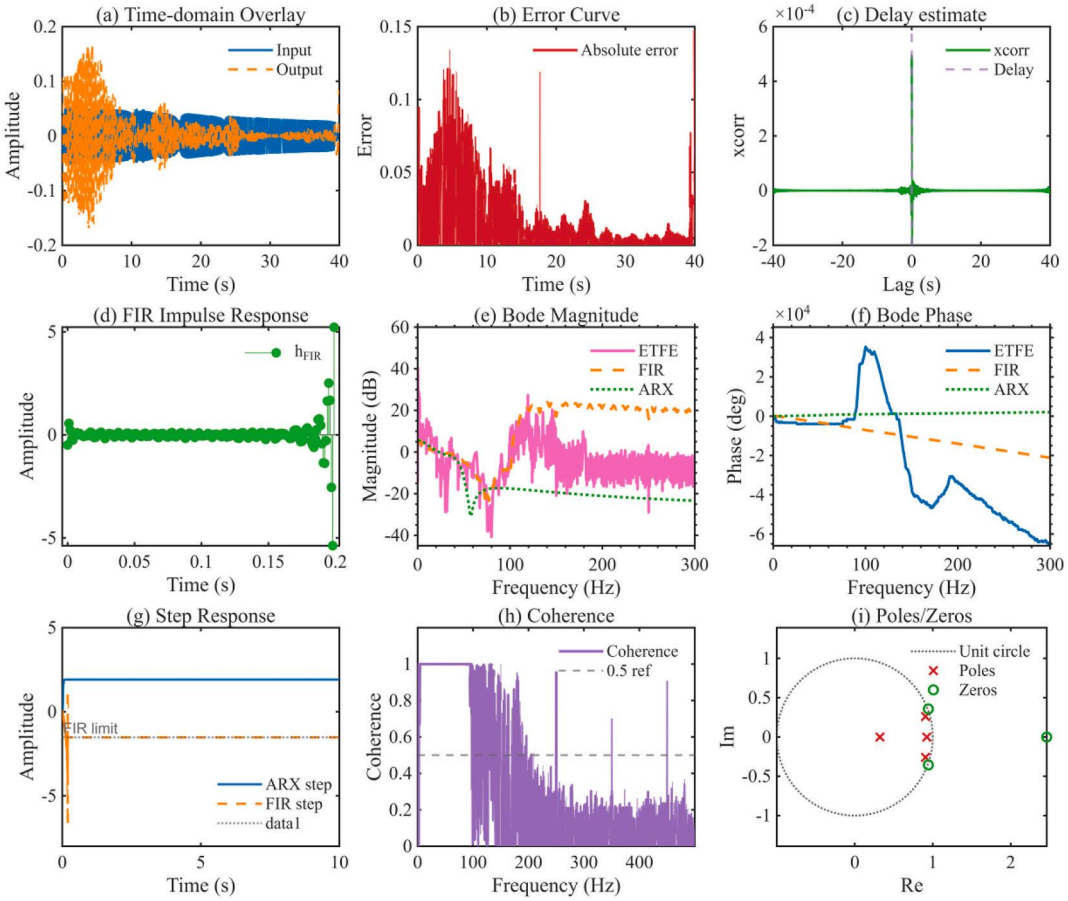

Fig. 8. Offline identification and dynamic characteristic analysis of the blade system.

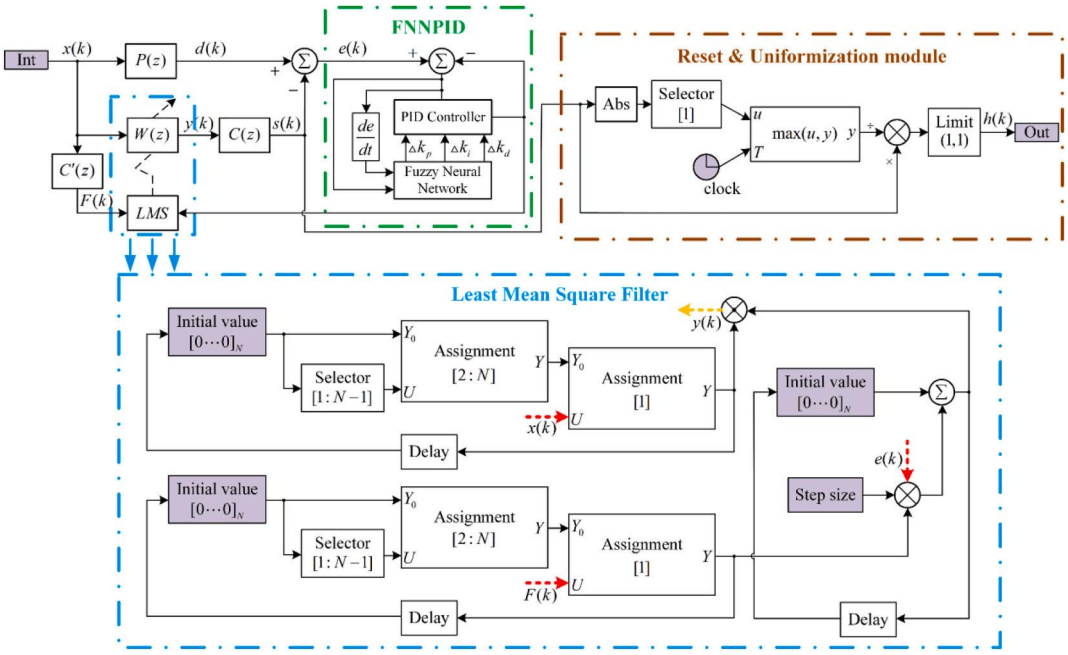

Fig. 9. Schematic diagram of the numerical simulation structure of the FNNPID-FxLMS algorithm.

nant resonant behavior and the main dynamic response relevant for controller design. A narrowband signal centered at the blade fundamental frequency was used as the system input. Based on the identified transfer function, numerical simulations of the FxLMS and FNNPID-FxLMS algorithms were conducted for control. The simulation results are shown in Fig. 10.

As shown in Fig. 10, the numerical simulation results of the traditional FxLMS control algorithm and the improved FNNPID-FxLMS control algorithm were compared. A comprehensive analysis was conducted on the time-domain response, power spectral density, phase plane, Poincaré section, as well as the cumulative probability distributions of error and amplitude. The results indicated that the FNNPID-FxLMS control algorithm generally outperformed the traditional FxLMS control in most evaluated aspects. Its advantages were particularly evident in the time-domain response, power spectral density reduction, and dynamic stability improvement. In the cumulative probability distribution of the control error, the improvement was comparatively moderate, but the proposed method still exhibited a more concentrated error distribution and a lower probability of large errors. Specifically, the FNNPID-FxLMS control not only significantly reduced system fluctuations in the time domain but also effectively decreased the peak values of power spectral density in the frequency domain, particularly within critical frequency ranges. In addition, the FNNPID-FxLMS control improved system stability by converging the dynamic trajectories and state points, and it effectively reduced control error and amplitude fluctuation, thereby enhancing the overall control accuracy of the system.

4.2. *Experimental results of active vibration and noise control for piezoelectric propeller blades*

The experimental work was divided into two operating conditions to simulate the vibration and noise radiation characteristics of the propeller under different scenarios. The first condition simulated the propeller under constant-speed propulsion, where the blade vibration was induced by unsteady hydrodynamic forces. These unsteady forces were typically generated by fluid turbulence, vortices, and the interactions between the propeller blades and the fluid. Such irregular force fluctuations caused the blades to undergo periodic or random vibrations during rotation. Blade vibration not only affected the propulsion efficiency of the propeller but also radiated intense low-frequency noise through blade–fluid interactions.

The second condition simulated the effect of transmitted vibrations from the shafting and the hull on the propeller. Specifically, the shafting transmitted the mechanical vibrations of the hull to the propeller through the drivetrain, while the interactions between the hull and the water also altered hull vibrations, which were further conducted through the shafting to the propeller. As a result, the blades generated multi-line vibrations. Such vibrations often exhibited more complex spectral features, characterized by multi-frequency vibration modes, and radiated broadband noise through the blades.

Through experimental analysis under these two conditions, a more comprehensive understanding of the vibration characteristics of the propeller and its radiated noise under different operating conditions was obtained, providing both data support and theoretical basis for subsequent propeller design and noise suppression technologies.

In both the numerical simulations and the experiments, the same control framework was adopted, and the main parameter settings were kept consistent to ensure comparability. The control step size was set to 1 ms. The adaptive learning rate and the initial PID parameters were selected within a stable range, and the representative values used in this study were 0.01, $k_p = 1.0$, $k_i = 0.1$, and $k_d = 0.01$, respectively. Saturation and normalization constraints were introduced in the algorithm to improve numerical stability and prevent excessive control output. The rated driving voltage of the piezoelectric ceramic actuator is 1000 V; however, during the actual control process, the actuator does not continuously operate at this maximum voltage amplitude, and the driving level varies with the control demand. The total power consumption of the piezoelectric driving system, including the power amplifier and supporting equipment, was approximately 7 W.

4.2.1. *Vibration and noise control experiment under constant-speed propulsion*

Flow–structure interaction analysis of the full-scale E1619 blade was carried out using Ansys Fluent. By performing simulations under different advance speeds, the dynamic responses of the blade under various operating conditions were obtained, and the corresponding axial unsteady force data were derived, as shown in Table 1.

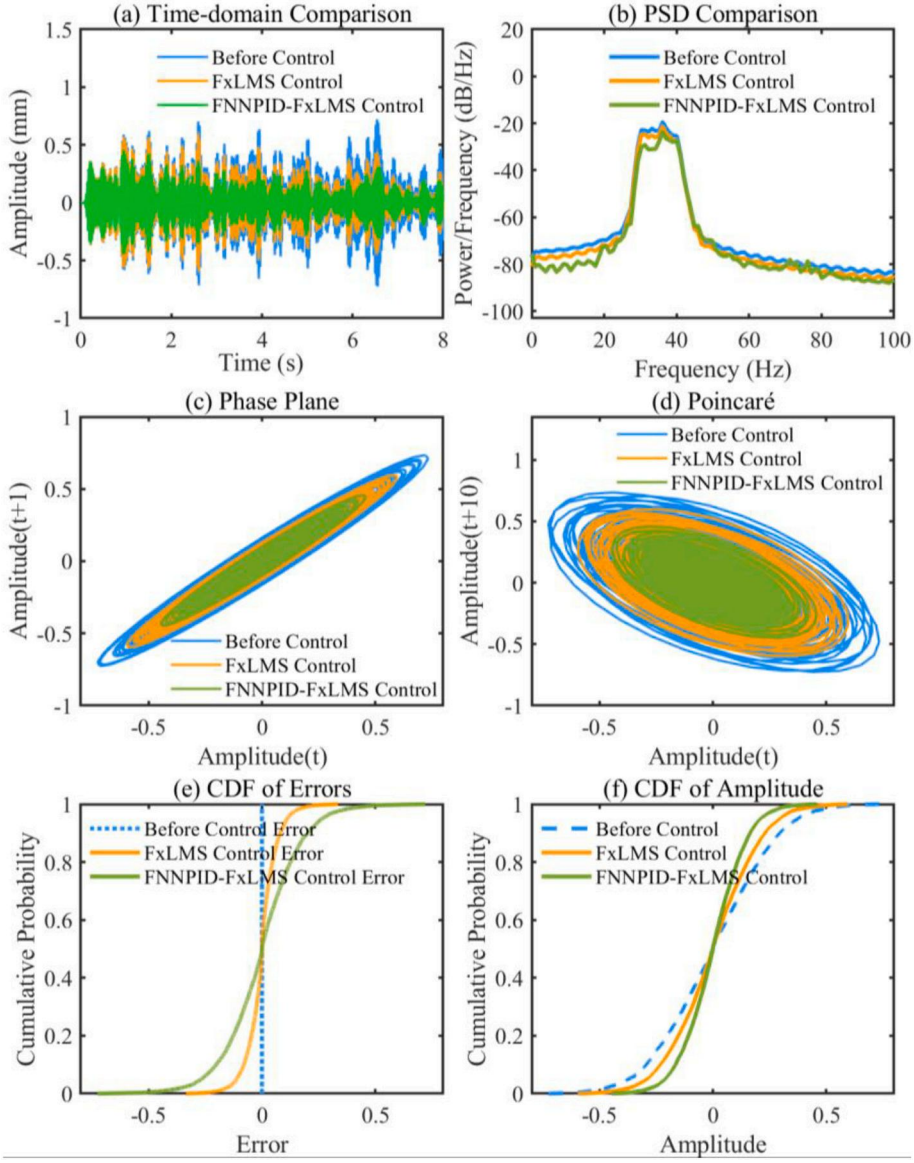

Fig. 10. Numerical simulation results.

Table 1
Axial unsteady force acting on the blade at different advance speeds.

Advance speed	Unsteady force
6 kn	11.5 N
12 kn	44.8 N
18 kn	99.5 N

The exciter functioned by applying excitation forces with different frequencies and amplitudes, thereby inducing blade vibration responses that matched the unsteady forces. The FNNPID-FxLMS algorithm was then used to control the vibration and noise of the blade. The exciter applied the unsteady force corresponding to the 6 kn advance speed at the fundamental frequency of the blade, simulating the dynamic behavior of the blade under actual operating conditions. The collected data were analyzed, as shown in Fig. 11.

As shown in Fig. 11, the control effect is most evident under the 6 kn condition. The blade vibration amplitude is substantially reduced in the time domain, and the dominant low-frequency vibration components are strongly suppressed in the frequency domain. The radiated noise is also reduced over the main frequency range, indicating that under relatively low advance speed, the proposed strategy is effective for both vibration suppression and the associated noise reduction.

The exciter applied the unsteady force corresponding to the 12 kn advance speed at the fundamental frequency of the blade, simulating the dynamic behavior of the blade under actual operating conditions. The collected data were analyzed, as shown in Fig. 12.

As shown in Fig. 12, the control strategy remains effective at 12 kn, but the improvement is less pronounced than that at 6 kn. The vibration response is still clearly reduced, and the dominant spectral peaks are weakened after control. In contrast, the noise reduction is more moderate, indicating that as the operating condition becomes stronger, the vibration suppression remains evident whereas the corresponding noise reduction becomes more condition-dependent.

The exciter applied the unsteady force corresponding to the 18 kn advance speed at the fundamental frequency of the blade, simulating the dynamic behavior of the blade under actual operating conditions. The collected data were analyzed, as shown in Fig. 13.

As shown in Fig. 13, under the advance speed of 18 kn, the control strategy still effectively reduced the blade vibration, while the noise reduction effect was comparatively limited. Although the noise levels at

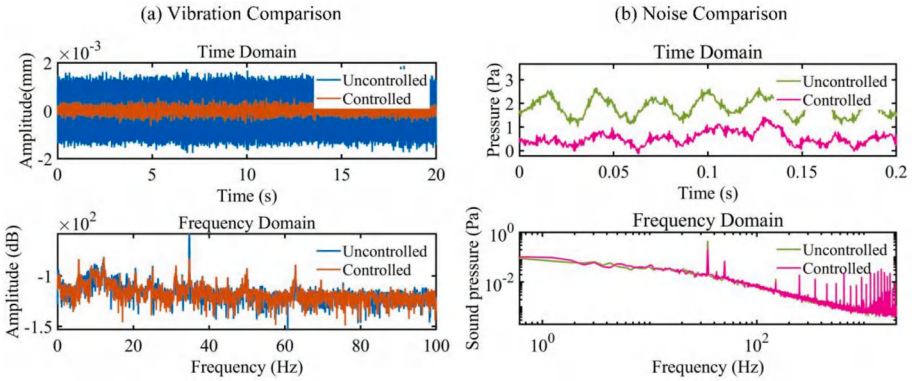

Fig. 11. Experimental results of vibration and noise control at an advance speed of 6 kn.

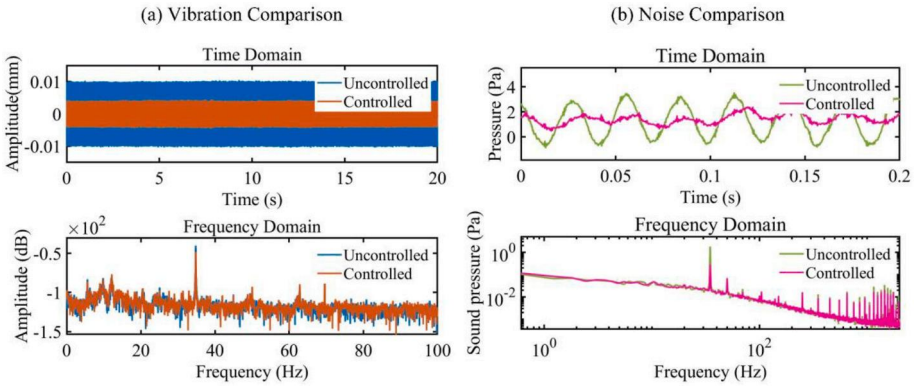

Fig. 12. Experimental results of vibration and noise control at an advance speed of 12 kn.

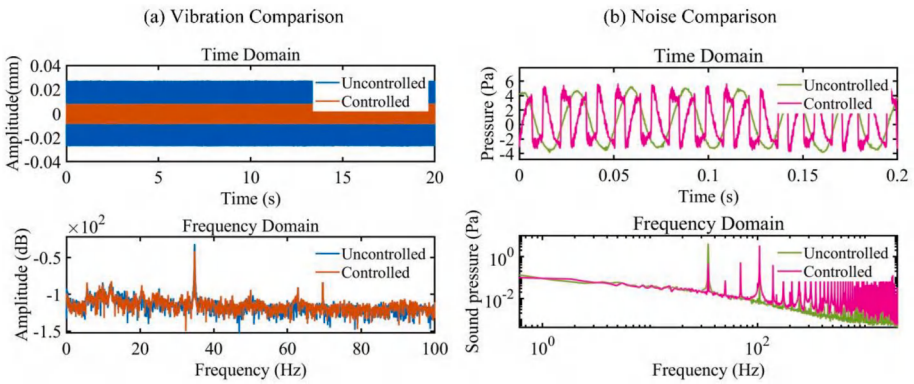

Fig. 13. Experimental results of vibration and noise control at an advance speed of 18 kn.

some characteristic frequency points were suppressed, the overall reduction in radiated noise was less significant than that under lower advance speeds. This is mainly because, under high-speed conditions, the vibration–acoustic coupling becomes more complex, and the acoustic energy tends to redistribute toward higher-order harmonic components after control. In terms of vibration, the vibration amplitude of the system was significantly reduced after control, and the vibration peaks in the frequency domain were effectively suppressed. In terms of noise, the control strategy lowered the noise levels at the characteristic frequency points of the system.

By simulating blade vibration and conducting control experiments under different advance speeds, the dynamic responses and control performance of the blade under various operating conditions were obtained. The vibration and noise of the blade under each condition were summarized and analyzed, as shown in Fig. 14.

As shown in Fig. 14, analysis of the vibration and noise control effects of the blade under different advance speeds demonstrated that the proposed control strategy significantly reduced both vibration and noise across all conditions. Specifically, under the advance speed of 6 kn, the root mean square (RMS) of blade vibration was reduced by 83.3%, while the noise RMS was reduced by 68.2%. At 12 kn, the vibration RMS was reduced by 60.1% and the noise RMS by 18.3%. At 18 kn, the vibration RMS was reduced by 66.5%, and the noise RMS was reduced by 6.4%, indicating that the control strategy was particularly effective in suppressing vibration and noise at lower advance speeds. After control, both vibration and radiated noise were reduced under most operating conditions; however, the degrees of reduction were not always consistent. This indicates that, although vibration and noise are coupled, the noise

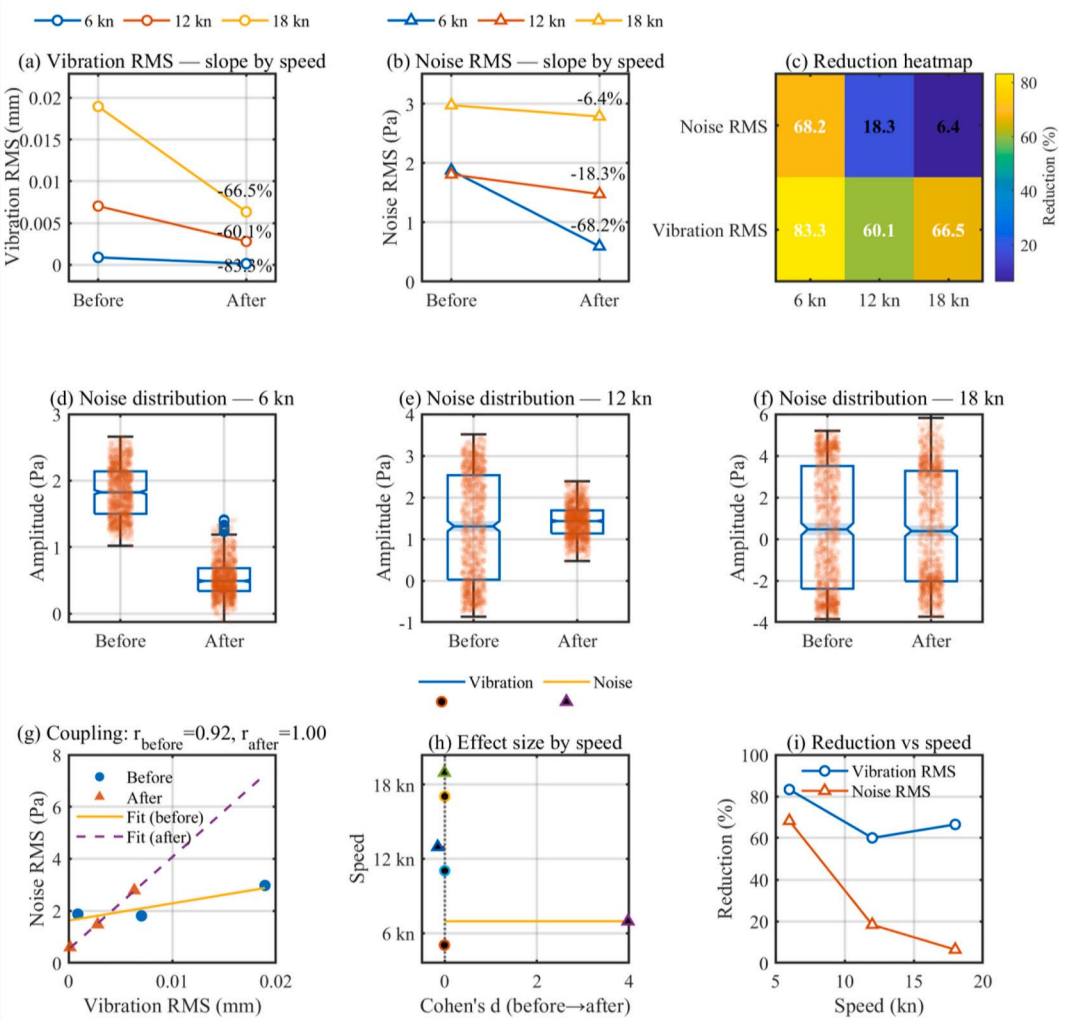

Fig. 14. Analysis of vibration and noise control results of the blade under constant-speed propulsion.

response is additionally affected by acoustic radiation characteristics and operating conditions. Therefore, the proposed strategy shows more

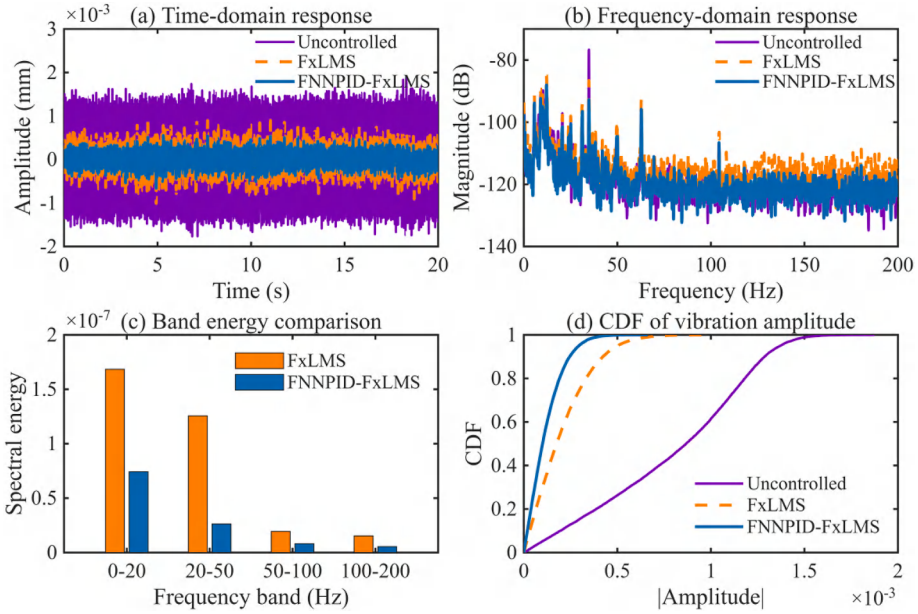

Fig. 15. Comparative control performance of the FxLMS and FNNPID-FxLMS algorithms under the 6 kn.

direct effectiveness in vibration suppression, while the noise reduction effect depends on the specific vibration–acoustic coupling state. Overall, the proposed control method effectively suppressed blade vibration and noise under different advance speeds, showing superior performance especially at lower speeds.

To further verify the experimental advantage of the proposed FNNPID-FxLMS algorithm over the traditional FxLMS algorithm, a vibration comparative test was carried out under the 6 kn condition, and the corresponding results are shown in Fig. 15.

Fig. 15 compares the control performance of the traditional FxLMS algorithm and the proposed FNNPID-FxLMS algorithm under the 6 kn condition. As shown in Fig. 15(a), both algorithms reduce the vibration response compared with the uncontrolled case, while the FNNPID-FxLMS algorithm achieves a smaller time-domain amplitude. Fig. 15 (b) shows that the proposed algorithm provides stronger suppression of the dominant vibration-related components in the frequency domain, especially in the low- and mid-frequency ranges. This trend is further confirmed in Fig. 15(c), where the spectral energy of the FNNPID-FxLMS algorithm is lower than that of the FxLMS algorithm in all selected frequency bands. In addition, the CDF results in Fig. 15(d) indicate that the vibration amplitude under the proposed algorithm is more concentrated within a smaller range, which reflects better control stability and robustness. These results demonstrate that the proposed FNNPID-FxLMS algorithm provides better overall vibration-control performance than the traditional FxLMS algorithm under the present operating condition.

4.2.2. *Vibration and noise control experiment under multi-line disturbances*

Under the multi-line disturbance conditions, the line-spectrum frequencies were selected as 5 Hz and its integer multiples, which enables simultaneous evaluation of the controller's performance under multi-line excitation and the system's stability when multiple harmonic disturbances exist. The amplitude of each harmonic component was approximately set according to the vibration levels observed under the 12 kn advance speed condition.

The exciter applied a disturbance force composed of two superimposed harmonic lines to the blade, simulating the possible dynamic behavior of the blade under actual operating conditions. The collected data were analyzed, as shown in Fig. 16.

As shown in Fig. 16, under the dual-line disturbance, the control strategy mainly suppresses the dominant low-frequency vibration components, resulting in a clear reduction in vibration amplitude. The noise response is also reduced, especially at the main concentrated spectral peaks. This result indicates that under relatively simple multi-frequency excitation, the proposed method can effectively attenuate both the structural vibration and its associated acoustic response.

The exciter then applied a disturbance force composed of four superimposed harmonic lines to the blade, simulating the possible dynamic behavior of the blade under actual operating conditions. The collected data were analyzed, as shown in Fig. 17.

As shown in Fig. 17, under the four-line disturbance, the vibration response after control becomes more stable, and multiple vibration peaks are simultaneously weakened. Compared with the dual-line case, the noise reduction is more pronounced in this condition, especially in the low- and mid-frequency ranges. This suggests that the proposed strategy has good adaptability under more complex multi-line excitation, particularly for noise suppression.

The exciter then applied a disturbance force composed of six superimposed harmonic lines to the blade, simulating the possible dynamic behavior of the blade under actual operating conditions. The collected data were analyzed, as shown in Fig. 18.

As shown in Fig. 18, under the six-line disturbance, the control strategy still provides stable vibration suppression, as reflected by the smoother waveform and the reduction of multiple spectral peaks. The noise response is also weakened after control; however, compared with the four-line case, the reduction is more distributed across different frequency components rather than concentrated at a few dominant peaks. This result reflects the increased complexity of the vibration–noise response under higher-order multi-line excitation.

The exciter then applied a disturbance force composed of eight superimposed harmonic lines to the blade, simulating the possible dynamic behavior of the blade under actual operating conditions. The collected data were analyzed, as shown in Fig. 19.

As shown in Fig. 19, under the eight-line disturbance, the uncontrolled system exhibits more complex vibration fluctuations, whereas the controlled response becomes noticeably more stable. The vibration amplitude is still reduced after control, indicating that the proposed method remains effective under highly complex excitation. The noise reduction is mainly reflected in part of the higher-frequency range, suggesting that under this condition the acoustic control effect is more selective and does not fully follow the vibration reduction trend.

By simulating blade vibration and conducting control experiments under multi-line disturbances, the dynamic responses and control performance of the blade under various operating conditions were obtained. The vibration and noise of the blade under each condition were summarized and analyzed, as shown in Fig. 20.

As shown in Fig. 20, the vibration RMS results indicated that the vibration amplitudes after control were significantly reduced as the number of spectral lines increased, demonstrating that the control strategy effectively suppressed vibration even at higher resolutions. The RMS of noise was also markedly reduced, with the most significant reductions observed under the four-line and six-line conditions. The maximum reduction in noise RMS reached 80.3% (at four lines), while the maximum reduction in vibration RMS reached 52.7% (at two lines). These results demonstrated the effectiveness of the control strategy in suppressing vibration and noise, as well as the differences in control performance under various resolutions.

Through the above analysis, the control strategy exhibited remarkable effectiveness under different numbers of spectral lines. The

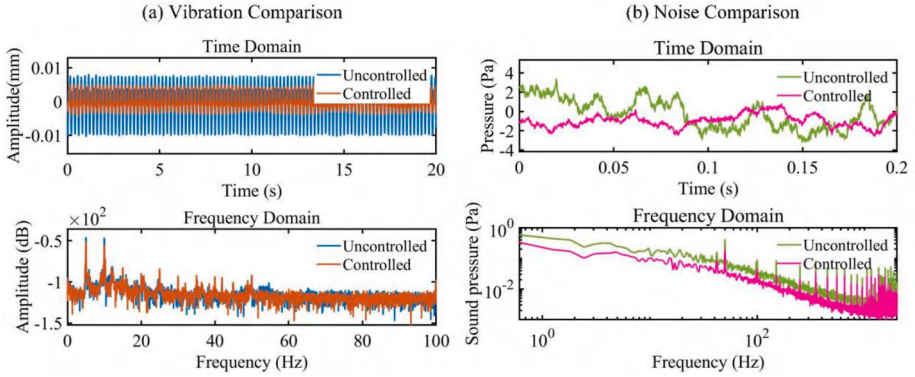

Fig. 16. Experimental results of vibration and noise control under dual-line disturbances.

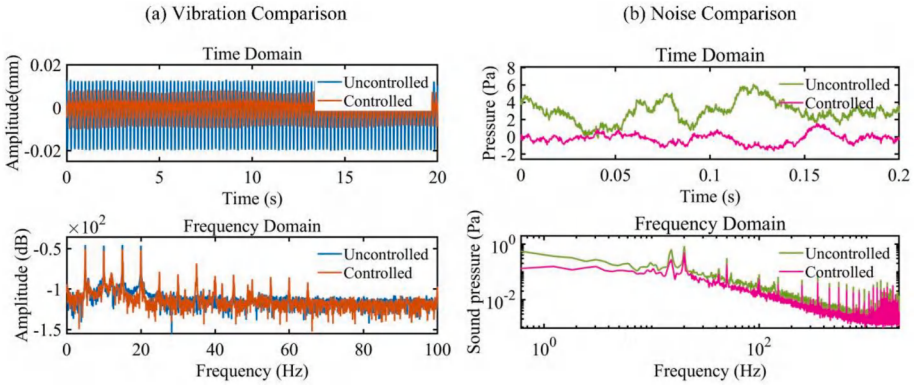

Fig. 17. Experimental results of vibration and noise control under four-line disturbances.

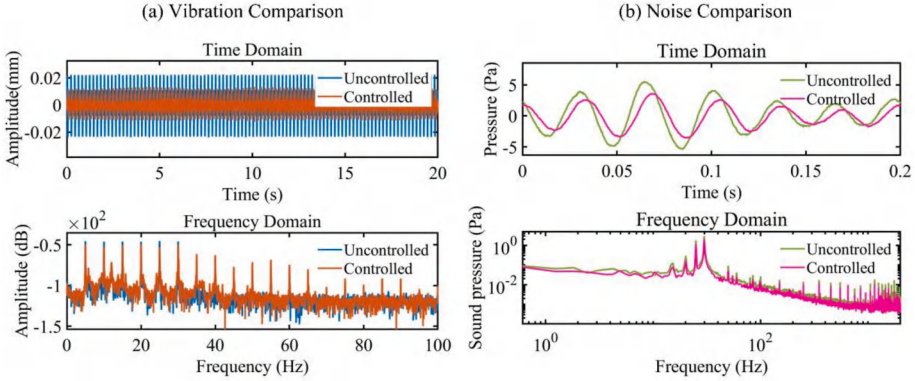

Fig. 18. Experimental results of vibration and noise control under six-line disturbances.

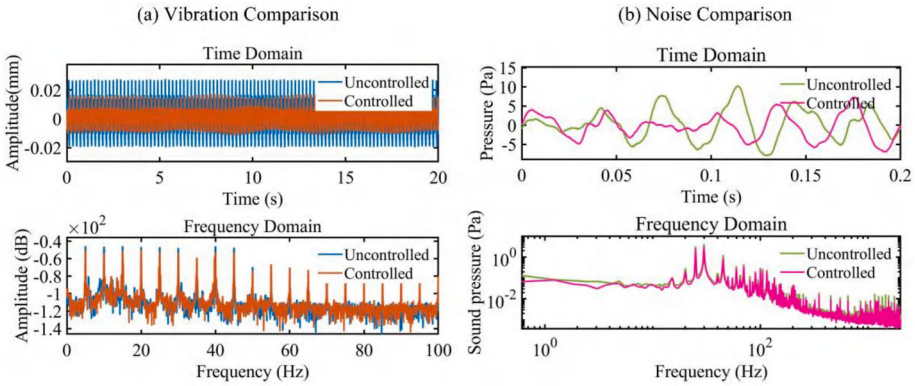

Fig. 19. Experimental results of vibration and noise control under eight-line disturbances.

reduction in vibration and noise reached more than 80% in some cases. After control, both vibration and noise distributions tended to become more concentrated in several tested cases. However, the reductions in vibration and noise were not always synchronized, indicating that their relationship is influenced by multiple factors, including modal characteristics and acoustic radiation efficiency. Therefore, the control strategy can be considered more robust for vibration suppression, while its effect on radiated noise shows stronger condition dependence. These findings provided valuable references for further optimization of vibration and noise control of marine propellers.

5. Conclusion

This study proposed and investigated an active vibration and noise control method for piezoelectric propeller blades based on the FNNPID-FxLMS algorithm. The effectiveness of the algorithm in suppressing blade vibration and noise under different operating conditions was verified through a combination of experiments and numerical simulations. Experimental results showed that the control system significantly reduced the vibration amplitude of the blades at various advance speeds, with particularly effective suppression in the low-frequency range. At the same time, radiated noise was also markedly improved, with the noise level in the high-frequency range effectively reduced. Specifically, under the condition of an advance speed of 6 knots, the root mean square (RMS) of vibration decreased by 83.3%, while the noise RMS decreased by 68.2%. At advance speeds of 12 and 18 knots, vibration remained significantly reduced, while the degree of noise reduction depended on the operating condition and was less pronounced at higher

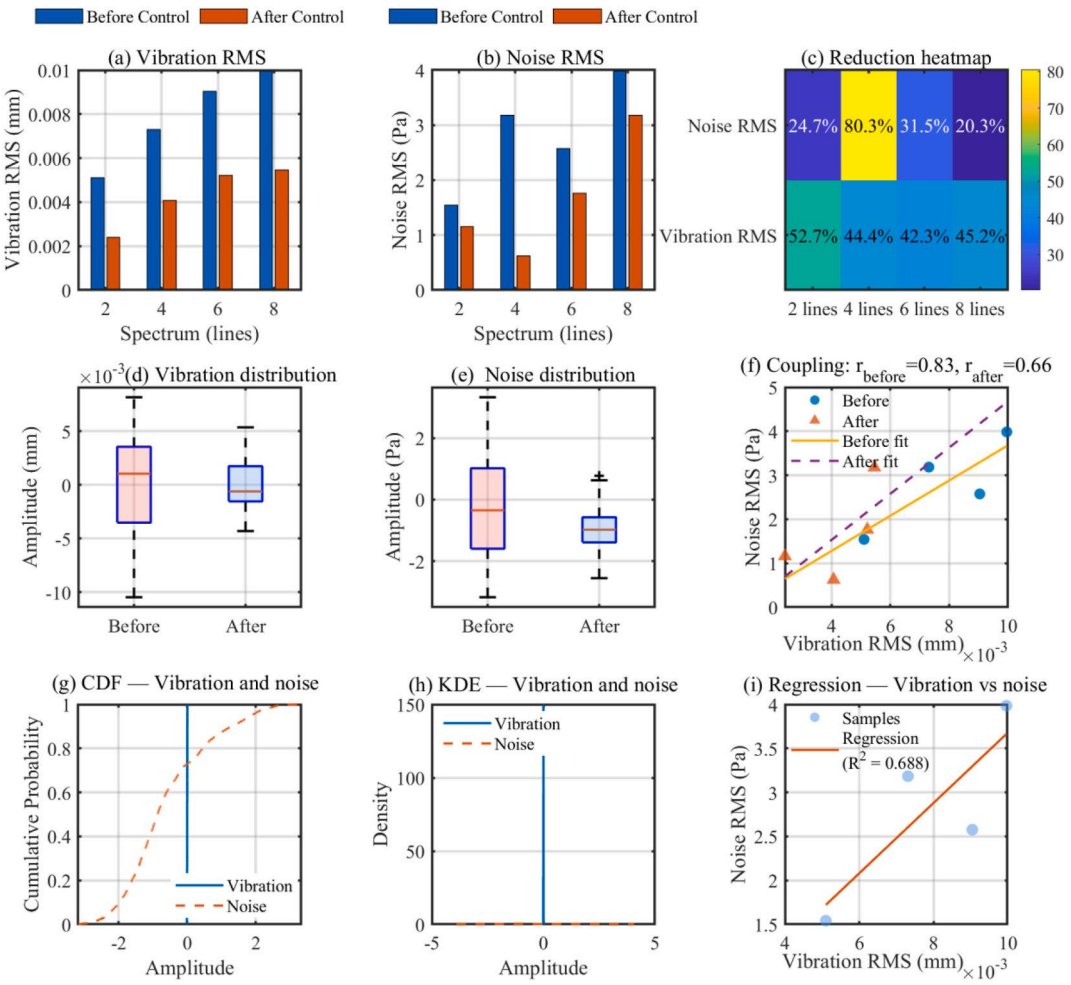

Fig. 20. Analysis of vibration and noise control results of the blade under multi-line disturbances.

speed.

In addition, analysis of vibration and noise control experiments under multi-line disturbances revealed that the control strategy effectively suppressed vibration and noise even at high resolutions. Moreover, under different numbers of spectral lines, the proposed strategy consistently improved vibration suppression, whereas the noise reduction performance varied with the disturbance condition.

In summary, the FNNPID-FxLMS algorithm, as a control method combining fuzzy PID control and adaptive filtering techniques, demonstrated significant advantages in the vibration and noise control of marine propellers. Its merits included faster convergence speed, lower steady-state error, and higher control accuracy, particularly when dealing with nonlinear and time-varying environments, where it provided excellent control performance. By effectively suppressing the coupling effect between vibration and noise, the method markedly improved system stability and accuracy, showing broad application prospects. Future research could further optimize the FNNPID-FxLMS algorithm and extend its application to more complex control scenarios, such as multi-channel coupled control and real engineering systems, in order to further enhance its control performance and applicability.

CRediT authorship contribution statement

Xudong Zhang: Writing – review & editing, Writing – original draft, Visualization, Investigation, Formal analysis, Conceptualization. **Pengxiang Zhao:** Writing – review & editing, Validation, Methodology, Data curation. **Xin Lan:** Writing – review & editing, Visualization, Validation, Data curation. **Weikai Shi:** Writing – review & editing, Visualization, Data curation. **Liwu Liu:** Writing – review & editing, Investigation, Conceptualization. **Yanju Liu:** Writing – review & editing, Investigation, Conceptualization. **Jinsong Leng:** Writing – review & editing, Supervision, Investigation.

Declaration of competing interest

The authors declare that they have no known competing financial interests or personal relationships that could have appeared to influence the work reported in this paper.

Acknowledgements

This work is supported by the National Natural Science Foundation of China (Grant No. 12272113).

References

A. Aboutiman, R. Shams, H.R. Karimi, et al., Active noise control in encapsulated structures with non-minimum phase characteristics using a Kalman filter approach, J. Sound Vib. 615, 119187.

K.G. Aktas, I. Esen, Dynamic response analysis and active vibration control of the smart sandwich composite plate with FGM core layers and MIMO FGPM actuators and sensors, IJMSD. 5 (1), 3-19.

K. Al-Souqi, K. Kadri, S. Emam, A review on vibration control using piezoelectric shunt circuits, Appl. Sci.-Basel. 15 (11), 6035.

F. Callipari, M. Sabatini, F. Angeletti, et al., Active vibration control of large space structures: modelling and experimental testing of offset piezoelectric stack actuators, Acta Astronaut. 198, 733-745.

K. Chai, Y.S. Liu, B.J. Hu, Multi-channel decentralized decoupling FxLMS algorithm and active vibration control experiment, J LOW FREQ NOISE V A. 43 (4), 1732-1760.
Y.Y. Chai, F.M. Li, Z.G. Song, et al., Analysis and active control of nonlinear vibration of composite lattice sandwich plates, Nonlinear Dyn. 102 (4), 2179-2203.
X.H. Chen, Y.X. Sun, M.H. Yu, et al., Theoretical and experimental study of active vibration control of rotating composite laminated beams using Fx-NLMS algorithm, Mech. Syst. Signal Process. 224, 111959.
C. Cheng, Z. Liu, X.L. Li, et al., An optimal sensor layout method based on noise reduction estimation for active road noise control, Mech. Syst. Signal Process. 220, 111668.
N.Y. Duan, C. Wu, Y.H. Huang, et al., Lateral vibration analysis and active control of the propeller-shafting system using a scaled experimental model, Ocean. Eng. 267, 113285.
Z.Y. Gao, Y. Lei, Z.M. Li, et al., Artificial piezoelectric metamaterials, Prog. Mater. Sci. 151, 101434.
Z.B. Geng, M. Chen, Y.J. Wang, et al., New multi-channel VSMFxLMS algorithm for vibration reduction of gear systems, Chin. J. Mech. Eng. 37 (1), 115.
Z.C. Huang, Y. Cheng, X.G. Wang, et al., Active vibration control and parameter optimization of genetic algorithm for partially damped composites beams, Biomimetics. 9 (10), 584.
M. Jalalnezhad, Design of intelligent control systems for damping vibrations of composite sheets using piezoelectricity as a sensor and actuator under various disturbance conditions, J. Braz. Soc. Mech. Sci. Eng. 47 (10), 495.
R. Jamshidi, A.A. Jafari, Nonlinear vibration of conical shell with a piezoelectric sensor patch and a piezoelectric actuator patch, J. Vib. Control. 28 (11–12), 1502-1519.
Y. Jiang, Y.C. Sun, Y.J. Shi, et al., Adaptive disturbance rejection control for vibration suppression of nonlinear flexible wings, Nonlinear Dyn. 113 (19), 26325-26339.
M. Kamaldar, N. Mohseni, S.A.U. Islam, et al., A numerical and experimental investigation of predictive cost adaptive control for noise and vibration suppression, Mech. Syst. Signal Process. 221, 111711.
T.Y. Li, C.L. Yu, X.Y. Yu, et al., Ultra-low frequency active vibration isolation system with quasi-zero stiffness characteristic using self-tuning filter-based feedforward control, J. Sound Vib. 597, 118848.
S.M. Li, Z.Y. Chen, Y.P. Ju, et al., Transverse vibration analysis and active disturbance rejection decoupling control of vector propulsion shaft system for underwater vehicles, Ocean. Eng. 298, 117158.
Y.Q. Lin, D.W. An, Z.Y. Lin, et al., Progress in high-performance stick-slip piezoelectric actuators: a review, Int J Smart Nano Mat. 15 (3), 652-696.
P.A.C. Lopes, J.A.B. Gerald, Careful feedback active noise and vibration control algorithm robust to large secondary path changes, Eur. J. Control. 75, 100905.
G.Q. Lu, R.W. Chen, H. Liu, Active noise control scheme for smart beds based on a wide and narrow band hybrid control algorithm, IEEE Access. 11, 92617-92627.
S.A. Luo, Y.B. Wang, X.H. Long, et al., Evaluation of FxLMS and FxRLS algorithms in active vibration control using piezoelectric stack actuators for gear transmission, Smart Mater. Struct. 34 (3), 035052.
A.G.A. Muthalif, K.A.M. Nor, A.N. Wahid, et al., Optimization of piezoelectric sensor-actuator for plate vibration control using evolutionary computation: modeling, simulation and experimentation, IEEE Access. 9, 100725-100734.
W. Ouyang, Q.L. Liu, J.J. Li, et al., Semi-active control for transverse vibration of ship propulsion shafting with magnetorheological squeeze film damper, Mech. Syst. Signal Process. 233, 112763.
M.H. Park, S. Yeo, J.H. Choi, et al., Review of noise and vibration reduction technologies in marine machinery: operational insights and engineering experience, Appl. Ocean Res. 152, 104195.
J. Przybylski, K. Kulinski, Nonlinear vibrations of a sandwich piezo-beam system under piezoelectric actuation, Nonlinear Dyn. 109 (2), 689-706.
S. Pulthasthan, H.R. Pota, The optimal placement of actuator and sensor for active noise control of sound-structure interaction systems, Smart Mater. Struct. 17 (3), 037001.
S.K. Sharma, R.C. Sharma, J.S. Lee, Propelling precision of longitudinal vibration mitigation in ship propeller shafts through advanced nonlinear intelligent semi-active control leveraging adaptive neuro-fuzzy inference system with linear quadratic regulator, J. Vib. Control. 31 (7–8), 1472-1484.
S.K. Sharma, R.C. Sharma, R.K. Upadhyay, et al., Coupled torsional-transverse vibration reduction in marine propulsion dynamics with novel approach using magnetorheological damping and adaptive control system, J. Vib. Eng. Technol. 12 (4), 6089-6099.
D. Singh, S. Sharma, R. Kumar, et al., Fuzzy logic based active vibration control using novel photostrictive composites, Compos. Struct. 313, 116919.
K. Singh, S. Sharma, R. Kumar, et al., Vibration control of cantilever beam using poling tuned piezoelectric actuator, Mech. Base. Des. Struct. Mach. 51 (4), 2217-2240.
C.S. Song, X.C. Xiong, Q. Yang, et al., Active vibration control using nonlinear auto-regressive neural network to identify secondary channel, J Low Freq Noise V A. 42 (4), 1803-1820.
L. Sujbert, Multiple reference active noise control - the attainable suppression, Appl. Acoust. 217, 109846.
Y.Q. Tian, C. Zhang, L. Yang, Active control of vibration and radiated noise in the shaft-shell coupled system of an underwater vehicle, Appl. Ocean Res. 154, 104324.
H.P. Wan, Q. Ma, G.S. Dong, et al., Data-driven model reduction approach for active vibration control of cable-strut structures, Eng. Struct. 302, 117434.
S.Q. Wang, H.C. Jin, Y. Wang, et al., Optimizing piezoelectric actuator placement for enhanced vibration control using genetic algorithms, Sci. Rep. 15 (1), 22340.
M. Watanabe, A. Prasad, Fractional delayed feedback for semi-active suspension control of nonlinear jumping quarter car model, Chaos Soliton Fract. 199, 116973.
M.Y. Wu, X.G. Liu, L. Dai, et al., Active vibration control of inlet piping system with a time-variant secondary path using the mirror modified filtered-x least mean square algorithm, J. Vib. Control. 30 (15–16), 3504-3515.
C.W. Wu, Z.G. Xiao, Y.T. Guo, et al., Analysis of nonlinear multi-field coupling responses of piezoelectric semiconductor rods via machine learning, Int J Smart Nano Mat. 15 (1), 62-74.
F. Xiong, Y. Li, J.C. Han, Method and experimental study of axial vibration suppression of propulsion shaft system supported by hybrid magnetic bearings, Ocean. Eng. 313, 119413.
S.F. Xu, X.X. Liu, Y.X. Wang, et al., Frequency shaping-based H∞ control for active pneumatic vibration isolation with input voltage saturation, Mech. Syst. Signal Process. 220, 111705.
A.P. Xu, Z.B. Xu, H. Zhang, et al., An adaptive feed-forward active vibration isolation algorithm for input disturbance unbalanced MIMO systems, Signal Process. 217, 109346.
J.H. Xu, X.L. Liu, Z.L. Xie, et al., Analysis and prediction of vibro-acoustic characteristics of parallel propulsion systems for large-scale marine ships, Appl. Ocean Res. 143, 103863.
Y.L. Yang, X.G. Liu, M.Y. Wu, et al., Multiple channel SPSA algorithm with improved cost function in active vibration control, Mech. Syst. Signal Process. 223, 111862.
J.A. Yang, J.L. Deng, J.H. Zhao, et al., A novel parallel multi-harmonic global multi-channel control algorithm for helicopter active vibration control, Control Eng. Pract. 142, 105772.
W.C. Yang, D.L. Yang, Z. Li, et al., Modal-based hybrid vibration control using friction and piezoelectric actuation for broadband frequency suppression, Int. J. Dyn. Control. 13 (5), 205.
H.Y. Yue, H.T. Xue, D.P. Yang, et al., Hybrid noise control in helicopter cabin with piezoelectric stack periodic strut, AIAA J. 63 (5), 1978-1992.
Zhang, Y.A., Zhu, S.Y., 2023. Novel model-free optimal active vibration control strategy based on deep reinforcement learning. Struct Control HLTH., 6770137
R.N. Zhang, L. Hyman, J.H. Ding, et al., Vibration suppression using piezoelectric actuator-based active flexure for, Mech. Syst. Signal Process. 235, 112816.
H. Zhang, W. Sun, Y. Zhang, et al., Dynamic modeling and active aeroelastic flutter control of functionally graded irregular plates with piezoelectric layers based on the discrete-coupling method, Thin-Walled Struct. 205, 112421.
C. Zhang, J. Ni, G. Wang, et al., A multi-channel active control scheme and its optimization for overall transverse vibration of a ship propulsion shaft system, Ocean. Eng. 332, 121468.
Y. Zhang, X.K. Guo, Y.F. Wu, et al., Active control of cables with piezoelectric actuation considering geometric and material nonlinearities, Eng. Struct. 340, 120773.
S. Zhang, L. Liu, X.M. Zhang, et al., Active vibration control for ship pipeline system based on PI-LQR state feedback, Ocean. Eng. 310, 118559.
S.S. Zhang, P. Jiang, J.X. Qi, et al., Adjustable indentation and vibration isolation performances of nacre-like metamaterial, Int J Smart Nano Mat. 14 (3), 303-320.
Y.Y. Zhang, Q.L. Liu, J.H. Wu, et al., Chaotic band-gap modulation mechanism for nonlinear vibration isolation systems based on time-delay feedback control, J. Phys. D Appl. Phys. 58 (1), 015311.